

Evolutions of CH₃CN abundance in molecular clumps

Zhen-Zhen He¹, Guang-Xing Li², Chao Zhang¹

¹ Department of Astronomy, Yunnan University, Kunming, 650091, China he_zhenzhen@foxmail.com

² South-Western Institute For Astronomy Research, Yunnan University, Kunming, 650091, China
gxli@ynu.edu.cn

Abstract To investigate the effects of massive star evolution on surrounding molecules, we select 9 massive clumps previously observed with the Atacama Pathfinder Experiment (APEX) telescope and the Submillimeter Array (SMA) telescope. Based on the observations of APEX, we obtain luminosity to mass ratio $L_{\text{clump}}/M_{\text{clump}}$ that range from 10 to 154 L_{\odot}/M_{\odot} , where some of them embedded Ultra Compact (UC) H II region. Using the SMA, CH₃CN (12_K–11_K) transitions were observed toward 9 massive star-forming regions. We derive the CH₃CN rotational temperature and column density using XCLASS program, and calculate its fractional abundance. We find that CH₃CN temperature seems to increase with the increase of $L_{\text{clump}}/M_{\text{clump}}$ when the ratio is between 10 to 40 L_{\odot}/M_{\odot} , then decrease when $L_{\text{clump}}/M_{\text{clump}} \geq 40 L_{\odot}/M_{\odot}$. Assuming the CH₃CN gas is heated by radiation from the central star, the effective distance of CH₃CN relative to the central star is estimated. The distance range from ~ 0.003 to ~ 0.083 pc, which accounts for $\sim 1/100$ to $\sim 1/1000$ of clump size. The effective distance increases slightly as $L_{\text{clump}}/M_{\text{clump}}$ increases ($R_{\text{eff}} \sim (L_{\text{clump}}/M_{\text{clump}})^{0.5 \pm 0.2}$). Overall, the CH₃CN abundance is found to decrease as the clumps evolve, e.g., $X_{\text{CH}_3\text{CN}} \sim (L_{\text{clump}}/M_{\text{clump}})^{-1.0 \pm 0.7}$. The steady decline of CH₃CN abundance as the clumps evolution can be interpreted as a result of photodissociation.

Key words: line: identification – stars: evolution – stars: formation – ISM: molecules – submillimeter: ISM

1 INTRODUCTION

Massive stars ($M \geq 8 M_{\odot}$) are formed inside molecular clouds. Feedback from star formation has substantial impacts on the evolution of the surround interstellar medium (ISM) through outflows, winds, as well as strong UV radiation (Garay & Lizano, 1999; Zinnecker & Yorke, 2007). Molecules, which have been detected in the ISM or circumstellar shells, are powerful tools to probe physical conditions such as densities, gas temperatures, and kinematical properties (Herbst & van Dishoeck, 2009).

Gerner et al. (2014) observed a sample of high-mass star-forming regions at different evolutionary

mass protostellar objects (HMPOs) to hot molecular cores (HMCs) and, finally, ultra-compact (UC) H II regions. They found that molecular species are rich in the HMC phase and decline for the UC H II stage. However, the evolution of high-mass star formation occurs on a short time scale and in a clustered environment (Bonnell et al., 2003). The transition from one stage to the next is not well-defined, there are some overlaps among those stages.

The collapse of molecular clump¹ is a global process: although the star formation that we observe occurs mostly at the center of the clumps, the actual collapse occurs on a much larger scale (e.g., Murray & Chang, 2015; Li, 2018). To study this collapse and the associated star formation, it is necessary to correlate the tracers of star formation with the properties of their natal clumps. A promising evolutionary indicator for massive and dense clumps is the L/M ratio – the ratio between the bolometric luminosity and the mass of the clump. Single dish investigations about the physical properties of star-forming regions at different L/M have been conducted in some works using molecules as probes (e.g., CH₃C₂H, CH₃CN, NH₃, CH₃OH; Molinari et al., 2016; Giannetti et al., 2017). These works show that the molecular temperatures are significantly changed in different physical conditions during stars formation.

CH₃CN (methyl cyanide) is known as a good tracer of warm and dense gas (e.g., Pankonin et al., 2001; Araya et al., 2005a; Giannetti et al., 2017). High spatial resolution observations seem to indicate that this molecule traces the disks around forming stars (Cesaroni et al., 1997; Keto & Zhang, 2010; Cesaroni et al., 2014; Chen et al., 2016; Sanna et al., 2019). Interferometric observations with high spatial resolutions are suitable for studying small regions as the CH₃CN emission mostly originates from small scales. Hernández-Hernández et al. (2014) searched the literature for MSFRs in the HMC phase observed using Submillimeter Array (SMA) and selected 17 sources. They studied the chemical properties of CH₃CN, and suggested that CH₃CN was formed in gas phase and their abundance was increased with the increase of temperature. In this paper, we tend to use the sources selected by Hernández-Hernández et al. (2014) and place these sources in the context of star evolution to study the influence of star formation on the surrounding molecules. Following Molinari et al. (2008), we propose to study star evolutionary stages indicated by the luminosity to mass ratios of the clumps.

2 DATA

2.1 Sample

Our samples are taken from Hernández-Hernández et al. (2014), who searched the literature for MSFRs in the HMC phase. Most of their sample sources are associated with UC H II regions. These sources were observed at a spatial scale of ~ 0.1 pc with similar observational resolution. We matched them with Atacama Pathfinder Experiment (APEX) Telescope Large Area Survey of the Galaxy (ATLASGAL; Schuller et al., 2009) dense clump catalogue based on their positions. The survey aims to provide a large and systematic list of clumps in the early embedded evolution stage. Nine massive clumps G5.89–0.39, G8.68–0.37, G10.62–0.38, G28.20–0.04N, G45.07+0.13, G45.47+0.05, IRAS 16547–4247, IRAS 18182–1433 and IRAS 18566+0408 are selected after removing some non-matched sources. The clump distances, effec-

¹ Following Zhang et al. (2009, 2015) in this paper, we tend to refer the size of cloud as 10 - 100 pc, the size of molecular clump as

Table 1: Clump properties

Source	Distance		Mass	Luminosity	$L_{\text{clump}}/M_{\text{clump}}$	R_{clump}
	kpc	M_{\odot}	$10^5 L_{\odot}$	L_{\odot}/M_{\odot}	pc	
G5.89–0.39	2.99	1698	2.11	124	0.653	
G8.68–0.37	4.45	2218	0.23	10	0.712	
G10.62–0.38	4.95	8649	5.21	60	1.584	
G28.20–0.04N	6.05	4446	1.30	29	1.349	
G45.07+0.13	8.00	3111	4.82	154	1.357	
G45.47+0.05	8.40	7161	4.30	59	2.078	
IRAS 16547–4247	2.74	1678	0.60	35	0.691	
IRAS 18182–1433	4.71	1342	0.18	13	0.708	
IRAS 18566+0408	4.86	1940	0.23	11	1.084	

Notes: Properties of our sample clumps taken by matching them to the sample of ATLASGAL (Urquhart et al., 2018).

tive radii, masses, and bolometric luminosities are taken from Urquhart et al. (2018). For our purpose, we use $L_{\text{clump}}/M_{\text{clump}}$ – the ratio between clump luminosity and mass – as the evolutionary indicator, and the 9 targets have $L_{\text{clump}}/M_{\text{clump}}$ ranging from 10 to 154 L_{\odot}/M_{\odot} . A summary of clump properties is presented in Table 1.

2.2 SMA observations and data reduction

The SMA observations were performed between April 2004 and January 2009. Selected targets are listed in Table 2, where observational epoch, frequency range, and spectral resolution are included. The correlator was set to the double-sideband receiver — the lower sideband (LSB) and the upper sideband (USB), each bandwidth is about 2 GHz. The rest frequencies of CH₃CN ($12_{\text{K}}-11_{\text{K}}$) are covered in the lower sideband. Spectral resolution is 0.406 MHz ($\sim 0.53 \text{ km s}^{-1}$) or 0.812 MHz ($\sim 1.1 \text{ km s}^{-1}$) for different sources. The system temperatures during those observations were less than 600 K.

Calibration and imaging are performed using the MIRIAD package² (Sault et al., 1995). Calibrators of bandpass, gain, and flux for each target are listed in Table 2. Considering the SMA monitoring of quasars, we estimate the fluxes uncertainty of $\sim 20\%$. We combined the continuum data from LSB and USB, the synthesized beam sizes range from $1.83'' \times 0.96''$ to $5.37'' \times 2.66''$. All the line data was regridded to a uniform spectral resolution of 0.812 MHz ($\sim 1.1 \text{ km s}^{-1}$).

3 RESULTS AND ANALYSIS

Hernández-Hernández et al. (2014) had completed the analysis of those data, they derived CH₃CN temperature and column density using a two-component method — a hot dense component and a warm extended component — by assuming different source size. In their results, the molecular abundances are mainly contributed from the hot dense components. In order to study the global variation of molecular abundance in star formation, we reanalysed selected data using single component fitting, the source size was derived by fitting CH₃CN (12_2-11_2) line emission region of each target (see Section 3.2), this method has been used in previous analysis (Beuther et al., 2006).

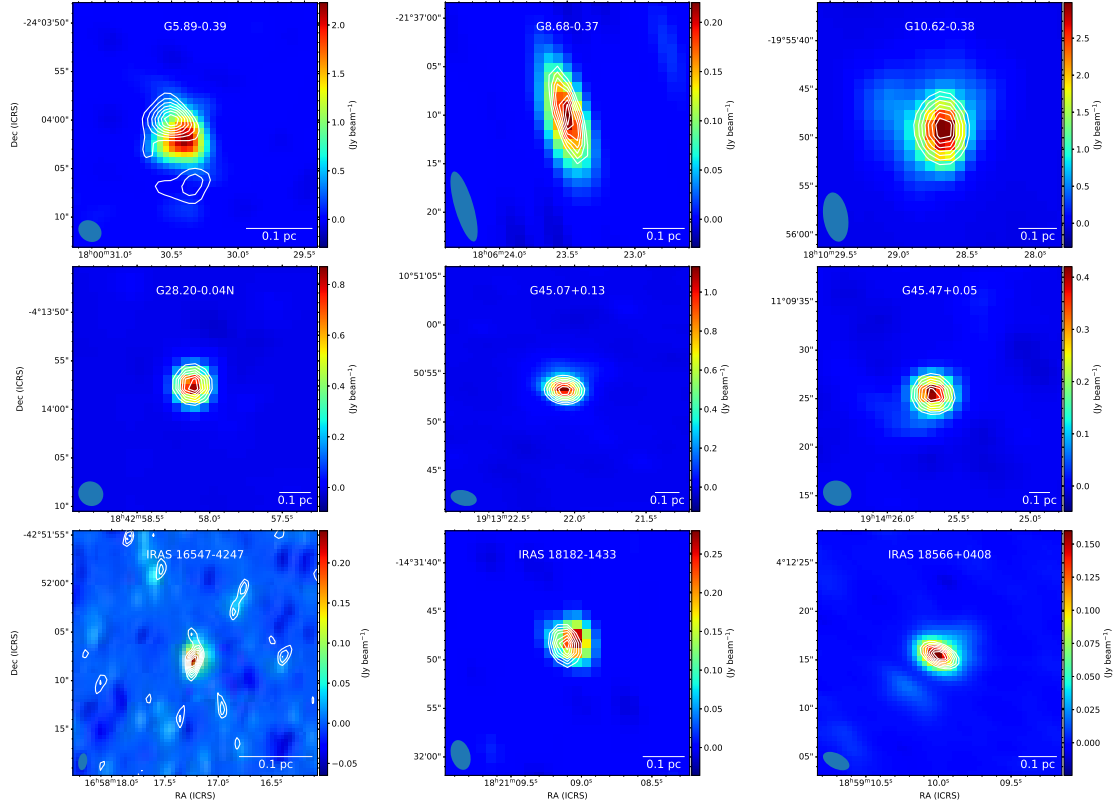


Fig. 1: 1.3 mm continuum images (color scale) and molecules line emission (white contours) of CH_3CN (12_2-11_2) toward massive star-forming regions. Contour levels have steps of 30%, 40%, 50%, 60%, 70%, 80%, until 90% of integrated emission. The synthesized beam of each source is shown at the bottom left. The 1.3 mm integrated emission flux of G5.89–0.39, G8.68–0.37, G10.62–0.38, G28.20–0.04N, G45.07+0.13, G45.47+0.05, IRAS 16547–4247, IRAS 18182–1433 and IRAS 18566+0408 is 7.50 Jy, 0.38 Jy, 6.86 Jy, 1.15 Jy, 1.63 Jy, 0.60 Jy, 0.56 Jy, 0.47 Jy, and 0.31 Jy, respectively, which are listed in Table 3.

3.1 Continuum

The continuum images, as shown in Figure 1, are constructed from line-free channels of LSB and USB in the visibility domain. The 1σ noise level of continuum is lower than 20 mJy beam^{-1} . Two-dimensional gaussian fittings are performed to obtain peak intensities, total flux densities, and deconvolved source sizes. The relevant results are listed in Table 3.

The 1.3 mm continuum emission may be contributed by free-free radiation and dust thermal radiation, because most HMCs harbor embedded UC H II regions. The free-free emission was obtained from Hernández-Hernández et al. (2014), who assumed the free-free emission is optically thin from 10 to 100 GHz and estimated the free-free emission by $S_\nu \propto \nu^{-0.1}$. The estimated dust continuum flux of each source is listed in Table 3.

To derive CH_3CN fractional abundance, we first calculate H_2 column densities for all observed regions. Assuming that the dust emission is optically thin, H_2 column density can be obtained by (Hildebrand, 1983; Lis et al., 1991):

$$N_{\text{H}_2} = 8.1 \times 10^{17} \frac{e^{h\nu/kT} - 1}{S_\nu} \left(\frac{\nu}{\text{cm}^{-2}} \right)^{-3} \quad (1)$$

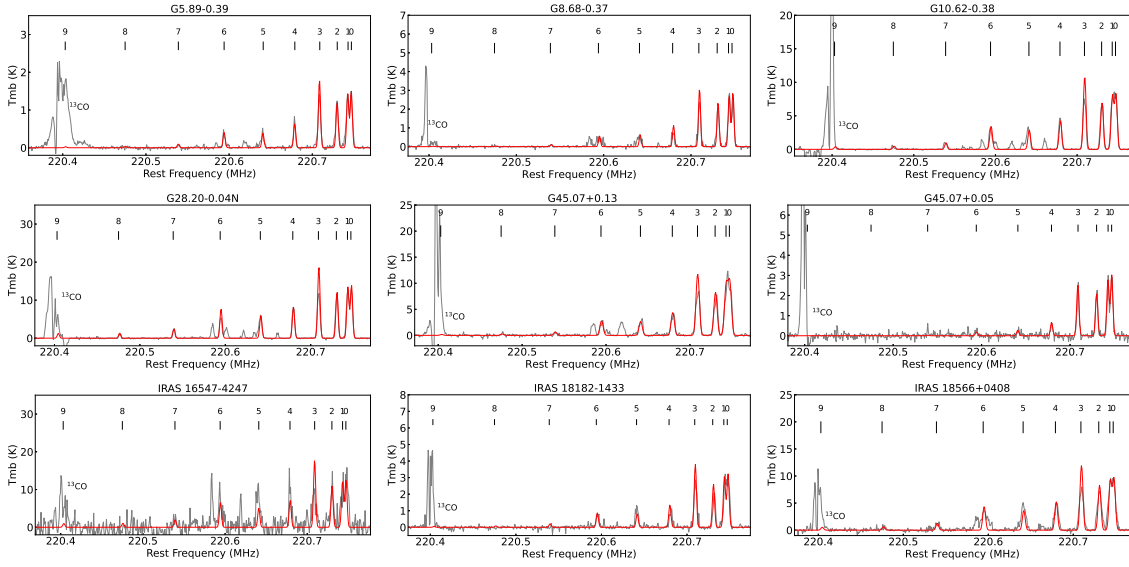


Fig. 2: Observed spectra (black) and model spectra (red) of CH₃CN (12_K-11_K). The model spectra are derived with XCLASS package. The number represent the K -ladder quantum numbers. The $K = 9$ line is overlapped with ^{13}CO (2-1) in some regions.

where k and h are the Boltzmann constant and Planck constant, respectively, T is the dust temperature, $Q(\nu)$ is the grain emissivity at frequency ν , Ω is the solid angle of source, S_ν is the total integrated flux of the dust continuum. We adopt $Q(\nu) = 2.2 \times 10^{-5}$ at 1.3 mm ($\beta = 1.5$; Lis & Goldsmith, 1990; Lis et al., 1991), and the gas-to-dust ratio of 100 is used. The dust temperature can be estimated from CH₃CN rotational temperature, which will be derived in Section 3.2, assuming that dust and gas are in thermal equilibrium (Kaufman et al., 1998). The derived H₂ column densities range from 0.39×10^{24} to 4.73×10^{24} cm⁻², the values are listed in Table 3.

Considering an absolute flux uncertainty of $\sim 20\%$ for SMA observations, dust temperature uncertainty of $\sim 20\%$, we estimate H₂ column density uncertainties of $\sim 50\%$ (Sanhueza et al., 2019). The H₂ column density we derived is comparable to the result of Hernández-Hernández et al. (2014). The difference may be caused by that they used the CH₃CN temperature of hot dense component to assume the dust temperature, while we derived a relatively low CH₃CN temperature using single component fitting. The H₂ column density is sensitive to dust temperature.

3.2 Molecular line emission

The spectral lines are extracted from the continuum peak position. Their continuum-subtracted spectra are plotted with intensity in units of Kelvin in Figure 2. The CH₃CN (12_K-11_K) lines are identified following Hernández-Hernández et al. (2014).

Spectral lines are modelled using the XCLASS package³ (Möller et al., 2017) to derive molecular temperature and column density. The modeling parameters are source size, rotational temperature, column density, line width, and velocity offset. The source sizes are obtained by two-dimension Gaussian fits to CH₃CN (12_2-11_2) line images. The 1σ noise level in line images are lower than 100 mJy beam⁻¹. The

line width and velocity offsets are obtained by Gaussian fitting. Those parameters are used as initial parameters. The optimization algorithm in MAGIX is used to explore the parameter space and minimize the χ^2 distribution space. The detailed fitting functions and modelling procedures are described in Möller et al. (2017), where local thermodynamical equilibrium (LTE) is assumed. The derived molecular temperature and column density are presented in Table 3.

We derive molecular fractional abundances relative to H_2 using $X = N_{\text{tot}}/N_{\text{H}_2}$, where N_{H_2} is the H_2 column density. CH_3CN rotational temperatures, column densities, and abundances are listed in Table 3. Both temperature and column density of CH_3CN obtained by our single component fitting are lower than yet comparable to that of the hot dense component and higher than that of the warm extended component obtained by Hernández-Hernández et al. (2014).

4 DISCUSSION

4.1 Evolutionary stages

The distribution of ATLASGAL sources in the luminosity-mass ($L_{\text{clump}}\text{-}M_{\text{clump}}$) plane are presented in Figure 3. This type of diagram has been used in the studies of low-mass and high-mass star-forming regions (e.g., Saraceno et al., 1996; Molinari et al., 2008; Giannetti et al., 2017), and can be used as a tool for separating different evolutionary stages. Evolutionary tracks were derived by Molinari et al. (2008), vertical and horizontal arrow refer to as the accretion and the envelope dispersion phases. Three lines of constant $L_{\text{clump}}/M_{\text{clump}}$ ratios (i.e., 1, 10 and $100 L_{\odot}/M_{\odot}$) are shown in figure. Our sources at different evolutionary stages are marked in Figure 3.

Based on previous studies, G8.68–0.37, IRAS 18182–1433, and IRAS 18566+0408 have no or weak continuum emission at centimeter observations (Longmore et al., 2011; Beuther et al., 2006; Araya et al., 2005b), and they are massive star forming regions at an early evolutionary stage before forming a significant UC HII region. Clumps reaching $L_{\text{clump}}/M_{\text{clump}} \sim 10 L_{\odot}/M_{\odot}$ are likely to stay in the transition phase between the main accretion phase and the dispersion phase (Giannetti et al., 2017). Most sources with $L_{\text{clump}}/M_{\text{clump}} \gtrsim 30 L_{\odot}/M_{\odot}$ are harboring UC HII regions (Su et al., 2009; Hunter et al., 1997; Afflerbach et al., 1994; Wood & Churchwell, 1989a), especially G5.89–0.39 and G45.07+0.13 have a $L_{\text{clump}}/M_{\text{clump}}$ in excess of $100 L_{\odot}/M_{\odot}$. G5.89–0.39 is an expanding shell-like UC HII region (Wood & Churchwell, 1989b). Recently, Zapata et al. (2019) have presented sensitive CO($J = 3-2$) observations that revealed the possible presence of an explosive outflow in G5.89–0.39. G45.07+0.13 is a pair of spherical UC HII regions, this region are interpreted as a shell generated by stellar wind (Turner & Matthews, 1984). A detailed description of each source is given in Hernández-Hernández et al. (2014).

Our sources have similar masses yet different luminosity-to-mass ratios. Taking advantage of this, we propose that our sources G8.68-0.37, IRAS 18566+0408, IRAS 18182-1433, G28.20-0.04N, IRAS 16547-4247, G45.47+0.05, G10.62-0.38, G5.89-0.39, and G45.07+0.13 form a sequence with $L_{\text{clump}}/M_{\text{clump}}$

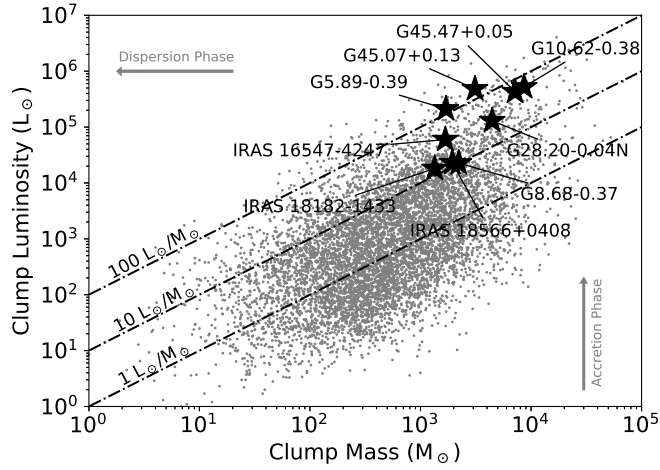


Fig. 3: Distribution of sources in the luminosity-mass plane. Stars represent selected sources in this paper. Gray dots represent the ATLASGAL clumps from Urquhart et al. (2018). The lower, middle and upper diagonal dash-dot lines indicate the $L_{\text{clump}}/M_{\text{clump}} = 1, 10$ and $100 L_{\odot}/M_{\odot}$, respectively. Vertical and horizontal arrow refer to as the accretion and the envelope dispersion phases derived by Molinari et al. (2008).

4.2 Temperature

In the upper left panel of Figure 4, we show the rotational temperature traced by CH₃CN gas as a function of the $L_{\text{clump}}/M_{\text{clump}}$. It seems that the temperature increases with $L_{\text{clump}}/M_{\text{clump}}$ when the ratio between 10 to $40 L_{\odot}/M_{\odot}$, and decreases when $L_{\text{clump}}/M_{\text{clump}}$ is greater than $40 L_{\odot}/M_{\odot}$. It is puzzling that rotational temperatures do not demonstrate a monotonic increase over the increase of L_{\odot}/M_{\odot} ratios. One would expect, in an idealized situation, that as a massive protostar gains masses and luminosity, the protostellar heating raises temperatures of the surrounding gas. Therefore, rotational temperatures are expected to increase with L_{\odot}/M_{\odot} ratios. This trend was observed by a single dish observations (e.g., Molinari et al., 2016; Giannetti et al., 2017; Urquhart et al., 2018). In these literatures, all molecular temperatures are considered to be continuously heated up when $L_{\text{clump}}/M_{\text{clump}} \gtrsim 10 L_{\odot}/M_{\odot}$.

Several factors may bias the data. The most direct influence on the observation results is the spatial resolution. The spatial resolution range of our 9 sources is from ~ 10000 to ~ 20000 AU, except for IRAS 16547–4247 with ~ 3000 AU. The $L_{\text{clump}}/M_{\text{clump}}$ of IRAS 16547–4247 is $35 L_{\odot}/M_{\odot}$, and it cannot result the decreasing trend of molecular temperature when $L_{\text{clump}}/M_{\text{clump}} > 40 L_{\odot}/M_{\odot}$. Thus the spatial dilution effect is not significant. Therefore, when $L_{\text{clump}}/M_{\text{clump}} > 40 L_{\odot}/M_{\odot}$, the decreasing trend of temperature is not caused by spatial resolution. The expansion of embedded UC H II regions might also affect the gas temperature. The $L_{\text{clump}}/M_{\text{clump}} \sim 10 L_{\odot}/M_{\odot}$ is considered a threshold that the birth of the zero age main sequence (Urquhart et al., 2014; Molinari et al., 2016; Giannetti et al., 2017), where hydrogen burning begins, then UC H II regions start to form and disperse the parent clumps (Hoare et al., 2007). Those processes may push ISM into the outer warm envelope, resulting a cavity located in the molecular clouds (e.g., G5.89, see Figure 1). Such an expansion of UC H II region may cause molecular temperature decrease

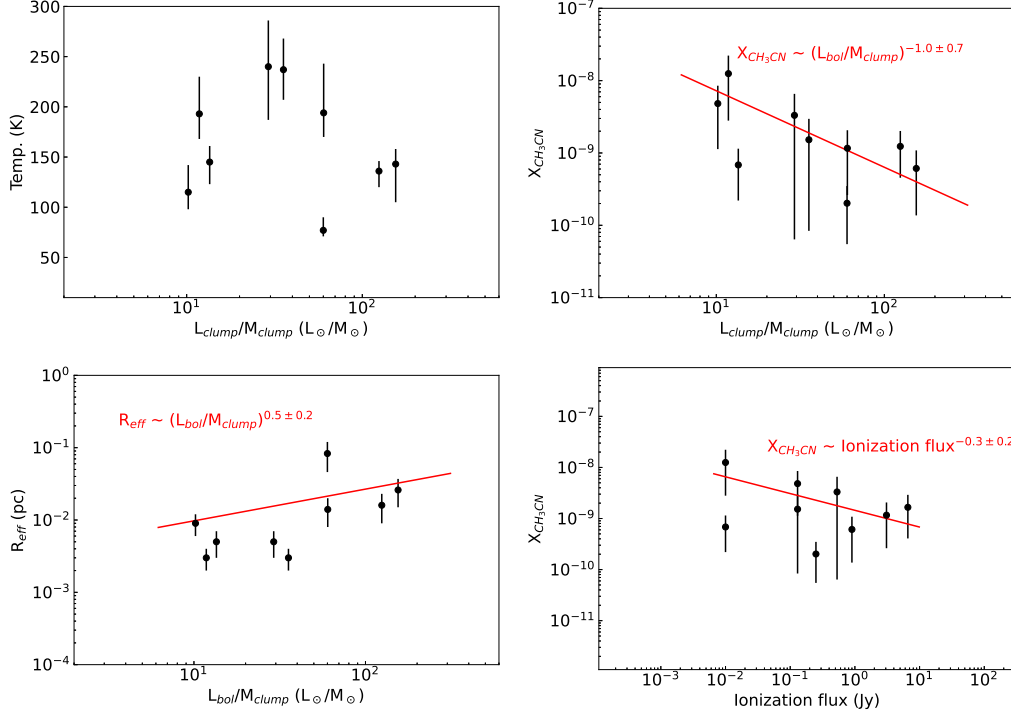


Fig. 4: **Upper left:** CH_3CN rotational temperature as a function of the $L_{\text{clump}}/M_{\text{clump}}$. Molecular temperatures are estimated with the XCLASS package. **Upper right:** CH_3CN abundance as a function of the $L_{\text{clump}}/M_{\text{clump}}$, the abundances are derived relative to H_2 column density. **Lower left:** Derived size ratios between CH_3CN effective distance R_{eff} as a function of the $L_{\text{clump}}/M_{\text{clump}}$. Molecular effective distance R_{eff} is derived based on molecular temperature and clump bolometric luminosity using $L = 4\pi R^2 \sigma T^4$. **Lower right:** CH_3CN abundance as a function of the ionization flux. The ionization flux at 1.3 mm was derived by Hernández-Hernández et al. (2014), who search for reported 10 to 100 GHz emission from the literatures and following $S_\nu \propto \nu^{-0.1}$.

4.3 Location of CH_3CN -emitting region

In Figure 1, the CH_3CN emission coincides with the 1.3 mm continuum emission, viewed at our current resolution. At the same time, we noticed that CH_3CN has a relatively complicated morphology in G5.89, where multiple dust continuum regions were found (Hunter et al., 2008).

Assuming that the gas is heated by the central star, molecular temperature is determined by radiative heating, molecular effective distance relative to the central heating source can be estimated by:

$$L = 4\pi R^2 \sigma T^4, \quad (2)$$

where R is the distance of the region with temperature T , the central source has bolometric luminosity L . We use this formula to estimate molecular effective distance R_{eff} , based on the bolometric luminosity of source, and on the molecular temperature derived in Section 3.2. Keto et al. (1987) studied the temperature scales of NH_3 gas in the vicinity of UC HII region G10.6-0.4, where the NH_3 gas temperature scales outward with a radius as $R^{-1/2}$.

The molecular effective distances were estimated using eq. 2 range from ~ 0.003 to ~ 0.083 pc, shown

relation between R_{eff} and $L_{\text{clump}}/M_{\text{clump}}$ in the lower left panel of Figure 4. According to our estimation, CH₃CN radiation should originate from $\sim 1/100$ to $\sim 1/1000$ of the ATLASGAL clump size and there is evidence for a correlation between the R_{eff} and $L_{\text{clump}}/M_{\text{clump}}$ where $R_{\text{eff}} \sim (L_{\text{clump}}/M_{\text{clump}})^{0.5 \pm 0.2}$. As the star evolves, the molecule is located relatively farther away from the central star.

4.4 CH₃CN abundance as an evolutionary tracer

In the upper right panel of Figure 4, we plot the relation between the molecular abundance and the $L_{\text{clump}}/M_{\text{clump}}$. It seems that the abundance decreases as $L_{\text{clump}}/M_{\text{clump}}$ increases, where a correlation of $X_{\text{CH}_3\text{CN}} \sim (L_{\text{clump}}/M_{\text{clump}})^{-1.0 \pm 0.7}$ can be found. CH₃CN is abundant in the early stage of HMC, and then the abundance decreases with the formation and evolution of UC H II region.

As stars evolve, they release more and more energy through UV radiation. Chemical model revealed that molecules have high column density at lower UV fields, while many species are photodissociated away for high UV fields (Stäuber et al., 2004). CH₃CN is subject to such photodissociation by UV radiation. The species whose abundances are enhanced are simple molecules including radicals and ions in photodissociated region (PDR), there are strong lines of simple species containing 2-4 atoms in W3 IRS4 (Helmich & van Dishoeck, 1997), supporting the photodissociation hypothesis. As shown in the bottom right of Figure 4, molecular abundance decreases with the increase of ionization flux ($X_{\text{CH}_3\text{CN}} \sim \text{Ionization flux}^{-0.3 \pm 0.2}$). It can also support the explanation of the decrease of molecular abundance caused by ionization.

5 CONCLUSION

We present SMA observations of 9 massive star-forming regions with $L_{\text{clump}}/M_{\text{clump}}$ ratios ranging from 10 to 154 L_{\odot}/M_{\odot} . We detect CH₃CN (12_K-11_K) lines in all sources, derive molecular temperatures and abundances, and study the relation between CH₃CN abundances and the evolutionary stage of sources measured in terms of luminosity-to-mass ratio $L_{\text{clump}}/M_{\text{clump}}$.

We find that the rotational temperatures of CH₃CN increase with the increase of $L_{\text{clump}}/M_{\text{clump}}$ when the ratio is between 10 to 40 L_{\odot}/M_{\odot} , then seem to decrease when $L_{\text{clump}}/M_{\text{clump}} \geq 40 L_{\odot}/M_{\odot}$, where the decline can be explained by dissipation. Assuming that the CH₃CN molecules are heated by radiation from the central stars, we estimated the effective distance of the CH₃CN relative to the central heating sources. Estimated CH₃CN effective distance range from ~ 0.003 to ~ 0.083 pc, which accounts for $\sim 1/100$ to $\sim 1/1000$ of clump size. The molecular effective distance R_{eff} increases slightly as $L_{\text{clump}}/M_{\text{clump}}$ increases ($R_{\text{eff}} \sim (L_{\text{clump}}/M_{\text{clump}})^{0.5 \pm 0.2}$).

We also find that the CH₃CN abundance is anti-correlated with $L_{\text{clump}}/M_{\text{clump}}$ where $X_{\text{CH}_3\text{CN}} \sim (L_{\text{clump}}/M_{\text{clump}})^{-1.0 \pm 0.7}$. They can be explained by photodissociation. CH₃CN abundance decrease when ionization flux was high. The strong anti-correlation deserves to be investigated with future high angular-resolution observations, and the relative abundance of CH₃CN might serve as a tracer for evolution in future

Table 2: Observational Parameters

Source	Observation Epoch	Frequency Range		Spectral Resolution MHz	Calibrators			Synthesized beam	
		LSB	USB		Bandpass	Gain	Flux	FWHM arcsec	P.A. deg
		GHz	GHz						
G5.89–0.39	2008 Apr 18	219.37–221.34	229.37–231.34	0.406	3C273	nrao530 1921–293	uranus	2.65 2.18	+54.0
G8.68–0.37	2008 Sep 17	220.28–222.27	230.28–232.27	0.406	3C454	nrao530 1911–201	uranus	7.86 1.99	+16.4
G10.62–0.38	2009 Jan 31	220.32–222.30	230.32–232.30	0.406	3C454	1733–130	uranus	5.37 2.66	+9.2
G28.20–0.04N	2008 Jun 21	220.25–222.22	230.25–232.22	0.406	3C454	1733–130 1911–201	uranus	2.77 2.59	+50.8
G45.07+0.13	2007 Apr 13	219.46–221.43	229.46–231.43	0.812	3C279	1751+096 1925+211	callisto	2.87 1.65	+77.5
G45.47+0.05	2008 Jun 30	219.15–221.13	229.15–231.13	0.406	3C279	1830+063 1925+211	callisto	3.11 2.69	+71.4
IRAS 16547–4247	2006 Jun 06	219.21–221.19	229.21–231.19	0.812	3C273	1745–290 1604–446	uranus	1.83 0.96	-7.5
IRAS 18182–1433	2004 Apr 30	219.37–221.34	229.37–231.34	0.812	3C273	nrao530 1908–201	uranus	3.19 2.00	+16.5
IRAS 18566+0408	2007 Jul 09	219.31–221.29	229.31–231.29	0.812	3C273	1751+096 1830+063	uranus	3.06 1.48	+60.6

References

- Afflerbach, A., Churchwell, E., & Hofner, P. 1994, in American Astronomical Society Meeting Abstracts, Vol. 184, American Astronomical Society Meeting Abstracts #184, 30.12
- Araya, E., Hofner, P., Kurtz, S., Bronfman, L., & DeDeo, S. 2005a, *ApJS*, 157, 279
- Araya, E., Hofner, P., Kurtz, S., et al. 2005b, *ApJ*, 618, 339
- Beuther, H., Zhang, Q., Sridharan, T. K., Lee, C. F., & Zapata, L. A. 2006, *A&A*, 454, 221
- Bonnell, I. A., Bate, M. R., & Vine, S. G. 2003, *MNRAS*, 343, 413
- Cesaroni, R., Felli, M., Testi, L., Walmsley, C. M., & Olmi, L. 1997, *A&A*, 325, 725
- Cesaroni, R., Galli, D., Neri, R., & Walmsley, C. M. 2014, *A&A*, 566, A73
- Chen, H.-R. V., Keto, E., Zhang, Q., et al. 2016, *ApJ*, 823, 125
- Garay, G., & Lizano, S. 1999, *PASP*, 111, 1049
- Gerner, T., Beuther, H., Semenov, D., et al. 2014, *A&A*, 563, A97
- Giannetti, A., Leurini, S., Wyrowski, F., et al. 2017, *A&A*, 603, A33
- Helmich, F. P., & van Dishoeck, E. F. 1997, *A&AS*, 124, 205
- Herbst, E., & van Dishoeck, E. F. 2009, *ARA&A*, 47, 427
- Hernández-Hernández, V., Zapata, L., Kurtz, S., & Garay, G. 2014, *ApJ*, 786, 38
- Hildebrand, R. H. 1983, *QJRAS*, 24, 267
- Hoare, M. G., Kurtz, S. E., Lizano, S., Keto, E., & Hofner, P. 2007, in *Protostars and Planets V*, ed. B. Reipurth, D. Jewitt, & K. Keil, 181
- Hunter, T. R., Brogan, C. L., Indebetouw, R., & Cyganowski, C. J. 2008, *ApJ*, 680, 1271
- Hunter, T. R., Phillips, T. G., & Menten, K. M. 1997, *ApJ*, 478, 283
- Kaufman, M. J., Hollenbach, D. J., & Tielens, A. G. G. M. 1998, *ApJ*, 497, 276
- Keto, E. R., Ho, P. T. P., & Haschick, A. D. 1987, *ApJ*, 318, 712
- Keto, E., & Zhang, Q. 2010, *MNRAS*, 406, 102
- Li, G.-X. 2018, *MNRAS*, 477, 4951
- Lis, D. C., Carlstrom, J. E., & Keene, J. 1991, *ApJ*, 380, 429
- Lis, D. C., & Goldsmith, P. F. 1990, *ApJ*, 356, 195
- Longmore, S. N., Pillai, T., Keto, E., Zhang, Q., & Qiu, K. 2011, *ApJ*, 726, 97
- Molinari, S., Merello, M., Elia, D., et al. 2016, *ApJ*, 826, L8
- Molinari, S., Pezzuto, S., Cesaroni, R., et al. 2008, *A&A*, 481, 345
- Möller, T., Endres, C., & Schilke, P. 2017, *A&A*, 598, A7
- Murray, N., & Chang, P. 2015, *ApJ*, 804, 44
- Pankonin, V., Churchwell, E., Watson, C., & Bieging, J. H. 2001, *ApJ*, 558, 194
- Sanhueza, P., Contreras, Y., Wu, B., et al. 2019, *ApJ*, 886, 102
- Sanna, A., Kölligan, A., Moscadelli, L., et al. 2019, *A&A*, 623, A77
- Saraceno, P., Andre, P., Ceccarelli, C., Griffin, M., & Molinari, S. 1996, *A&A*, 309, 827
- Sault, R. J., Teuben, P. J., & Wright, M. C. H. 1995, in *Astronomical Society of the Pacific Conference Series*, Vol. 77, *Astronomical Data Analysis Software and Systems IV*, ed. R. A. Shaw, H. E. Payne, & J. J. E. Hayes, 433

- Schuller, F., Menten, K. M., Contreras, Y., et al. 2009, *A&A*, 504, 415
- Stäuber, P., Doty, S. D., van Dishoeck, E. F., Jørgensen, J. K., & Benz, A. O. 2004, *A&A*, 425, 577
- Su, Y.-N., Liu, S.-Y., Wang, K.-S., Chen, Y.-H., & Chen, H.-R. 2009, *ApJ*, 704, L5
- Turner, B. E., & Matthews, H. E. 1984, *ApJ*, 277, 164
- Urquhart, J. S., Moore, T. J. T., Csengeri, T., et al. 2014, *MNRAS*, 443, 1555
- Urquhart, J. S., König, C., Giannetti, A., et al. 2018, *MNRAS*, 473, 1059
- Wood, D. O. S., & Churchwell, E. 1989a, *ApJ*, 340, 265
- Wood, D. O. S., & Churchwell, E. 1989b, *ApJS*, 69, 831
- Zapata, L. A., Ho, P. T. P., Guzmán Ccolque, E., et al. 2019, *MNRAS*, 486, L15
- Zhang, Q., Wang, K., Lu, X., & Jiménez-Serra, I. 2015, *ApJ*, 804, 141
- Zhang, Q., Wang, Y., Pillai, T., & Rathborne, J. 2009, *ApJ*, 696, 268
- Zinnecker, H., & Yorke, H. W. 2007, *ARA&A*, 45, 481

Table 3: Derived parameters

Source	1.3 mm Continuum Results						Derived CH ₃ CN parameters					
	S _ν ^{Peak} Jy beam ⁻¹	S _ν ^{Total} Jy	S _ν ^{Dust1} Jy	θ _s ² arcsec	rms mJy beam ⁻¹	N _{H2} ³ 10 ²⁴ cm ⁻²	θ _m ⁴ arcsec	rms mJy beam ⁻¹	T _{rot} K	N _{tot} cm ⁻²	X	R _{eff} ⁵ pc
5.89–0.39	2.23±0.07	7.50±0.29	0.91±0.46	3.90×3.24	11.26	0.70	5.4	39.02	147 ⁺¹⁷ ₋₁₂	8.63 ^{+1.3} _{-1.0} (14)	1.23±0.78(-9)	0.016±0.007
8.68–0.37	0.22±0.01	0.38±0.01	0.25±0.01	3.67×2.20	0.58	0.39	1.2	15.65	115 ⁺²⁷ ₋₁₇	1.88 ^{+0.5} _{-0.6} (15)	4.82±3.69(-9)	0.009±0.003
10.62–0.38	2.98±0.12	6.86±0.37	3.78±1.02	4.33×2.96	3.21	2.16	2.4	15.47	194 ⁺⁴⁹ ₋₂₄	2.51 ^{+0.8} _{-0.6} (15)	1.16±0.90(-9)	0.014±0.006
28.20–0.04N	0.87±0.01	1.15±0.01	0.62±0.21	1.73×1.12	1.50	1.88	1.4	31.50	240 ⁺⁴⁶ ₋₅₃	6.23 ^{+2.5} _{-3.6} (15)	3.31±3.25(-9)	0.005±0.002
45.07+0.13	1.13±0.03	1.63±0.07	0.73±0.42	1.31×1.18	4.09	4.73	1.3	31.14	143 ⁺¹⁵ ₋₃₈	2.89 ^{+0.3} _{-1.4} (15)	6.10±4.74(-10)	0.026±0.011
45.47+0.05	0.42±0.01	0.60±0.02	0.35±0.09	2.02×1.55	2.18	2.15	1.5	30.12	77 ⁺¹³ ₋₆	4.34 ^{+1.2} _{-0.9} (14)	2.01±1.47(-10)	0.083±0.037
RAS 16547–4247	0.24±0.01	0.56±0.03	0.43±0.07	1.39×1.25	19.81	1.47	1.9	93.34	237 ⁺³¹ ₋₃₀	2.24 ^{+1.3} _{-0.7} (15)	1.52±1.44(-9)	0.003±0.001
RAS 18182–1433	0.28±0.01	0.47±0.01	0.46±0.01	2.37×1.17	1.09	1.64	1.4	14.22	145 ⁺¹⁶ ₋₂₂	1.12 ^{+0.3} _{-0.2} (15)	6.82±4.63(-10)	0.005±0.002
RAS 18566+0408	0.16±0.01	0.31±0.02	0.30±0.01	2.10×1.80	2.08	0.58	1.2	28.85	193 ⁺³⁷ ₋₂₅	7.25 ^{+1.4} _{-2.9} (15)	1.25±0.97(-8)	0.003±0.001

¹ S_ν^{Dust} = S_ν^{Total} – S_ν^{free-free}. The free-free emission was obtained from Hernández-Hernández et al. (2014), who assumed the free-free emission is optically thin from 10 to 100 GHz and estimated the free-free emission by S_ν ∝ ν^{-0.1}.

² Deconvolved continuum sizes from 2D gaussian fit.

³ H₂ column density derived from the estimated 1.3 mm dust continuum emission (S_ν^{dust}) assuming T_{dust} = T_{CH₃CN}.

⁴ Deconvolved molecular distribution sizes from 2D gaussian fit.

⁵ Effective distance of the CH₃CN-emitting region is calculated using $L = 4\pi R^2 \sigma T^4$. T is the temperature of the CH₃CN gas and L is clump bolometric luminosity.